Proceedings of the IASS Annual Symposium 2025
"The living past as a source of innovation"
October 27 – 31, 2025, México City, México
Juan Gerardo Oliva, Juan Ignacio del Cueto, Elisa Drago Quaglia (eds.)

Advanced Finite Element Modeling of 3D-Printed Post-Tensioned Concrete Beams with Experimental Validation

Fahimeh YAVARTANOO^a, Damon BOLHASSANI^{a*}, Masoud AKBARZADEH^b, Maximilian E. ORORBIA^b, Hua CHAI^b, Yefan Zhi^b, Ibrahim ALACHEK, Leon TROUSSET^c, Mylene BERNARD^c, Karolina PAJAK^c

*, a ABC Lab, Spitzer School of Architecture, The City College of New York (CCNY), New York, USA * mbolhassani@ccny.cuny.edu

^b Polyhedral Structures Laboratory, Weitzman School of Design, University of Pennsylvania, Philadelphia, USA ^c SIKA, Zurich, Switzerland

Abstract

This study presents a numerical modeling framework for analyzing the structural behavior of 3D-printed post-tensioned concrete structures. A finite element (FE) model was developed in ABAOUS to simulate the nonlinear mechanical response of a 10-meter segmented canopy, which comprises nine 3D-printed concrete segments. The modeling approach was first validated using three small-scale post-tensioned beams (each approximately 1 meter in length, consisting of five segments) before being extended to the full-scale canopy. The numerical model incorporates a homogenized material representation for 3Dprinted concrete, employing a concrete damage plasticity (CDP) model to capture inelastic behavior and damage evolution. Post-tensioning steel cables were modeled as solid elements with linear elastic properties, while contact interactions were precisely defined to represent the interface between concrete segments and post-tensioning tendons. Boundary conditions and loading scenarios were carefully implemented to replicate experimental configurations. The simulations were conducted using a static general analysis scheme with nonlinear geometry to account for large deformations and material nonlinearities. Model calibration was performed through comparative analysis with experimental data from full-scale testing conducted at CERIB, refining key parameters such as material properties, interface behavior, boundary constraints, and load application methods. The validated FE analysis accurately models stress distribution, deformation characteristics, and structural performance, demonstrating strong correlation with experimental observations. The findings confirm the efficacy of the FE model in capturing the structural response of 3D-printed, post-tensioned concrete structures, offering a computationally efficient and reliable methodology for evaluating their mechanical behavior.

Keywords: 3D-printed post-tensioned concrete, Finite element analysis, Concrete damage plasticity (CDP) model, FE model, Numerical validation, Calibration, ABAQUS.

1. Introduction

The construction industry is among the largest contributors to environmental degradation, accounting for nearly 37% of global CO₂ emissions [1–3]. These emissions stem from the production of energy-intensive materials, particularly cement, as well as on-site construction activities, transportation, and operational energy use [4]. Traditional methods of concrete construction rely on large quantities of single-use formwork and manual labor, resulting in material waste, dust pollution, and significant energy

consumption across the project lifecycle. In response to these challenges, additive manufacturing (AM) technologies, particularly three-dimensional concrete printing (3DCP), have emerged as sustainable alternatives. 3DCP enables the automated, layer-by-layer fabrication of structural elements with minimal formwork and reduced material waste [5–7]. It also offers new architectural possibilities through the creation of complex geometries that would be difficult or costly to achieve with conventional methods.

Despite these advantages, the structural performance of printed concrete remains a key concern. The anisotropic, layered nature of 3D printing and lack of embedded reinforcement can lead to reduced tensile capacity and interlayer bond strength, limiting the application of printed concrete structures to load-bearing systems. To improve mechanical behavior, recent research has explored the integration of reinforcement systems into the 3D printing process. Among these, post-tensioning has shown particular promise. By applying compressive stresses to counteract tensile forces, post-tensioning enhances crack resistance, stiffness, and overall load capacity of printed concrete members. Bai et al. [8] investigated 3DP-UHPC composite beams with localized post-tensioning and demonstrated improvements in stiffness and ultimate strength. Raza et al. [9] examined 3D printed ribbed formworks under eccentric axial post-tensioning, reporting enhanced deformation control and load transfer capabilities. The application of post-tensioning in modular and prefabricated systems has also gained attention. Laccone et al. [10] proposed a segmented concrete shell system using 3D printed molds and optimized cable networks, reducing internal tension forces by up to 86.6% and enabling lightweight, formwork-free assembly. Miri et al. [11] reviewed large-scale 3D printed bridge components and concluded that posttensioning significantly improves both short-term performance and long-term durability, especially in prefabricated modular designs.

Nevertheless, modeling such hybrid systems remains complex due to the nonlinear behavior of printed concrete, interfacial contact mechanisms, and the influence of geometric discontinuities. Accurately simulating damage evolution and tendon-concrete interaction is essential for predicting structural behavior. To address these challenges, this study presents a finite element analysis of a full-scale 3D printed post-tensioned concrete beam using the Concrete Damaged Plasticity (CDP) model in ABAQUS [12]. The analysis incorporates realistic material properties, tendon configuration, and continuous geometry to assess load response, damage propagation, and failure mechanisms, contributing to the growing body of knowledge on structurally optimized, digitally fabricated concrete systems.

2. Methodology

2.1. Design and fabrication

A prototype funicular concrete beam was developed through an integrated computational workflow that synthesizes equilibrium-based form-finding with volumetric modeling, while explicitly considering fabrication constraints [13, 14, 22]. The design process began with generating a hybrid tension-compression form using polyhedral graphic statics to establish a geometry in structural equilibrium under combined loading [14]. This geometry was then modified to include periodic anticlastic surface (PAS) features for improved structural efficiency and compatibility with extrusion-based 3D concrete printing. To enable post-tensioning, internal voids were embedded within the beam's tensile zones, as determined by the funicular form. The design incorporated constraints specific to 3D printing, such as slicing direction, toolpath continuity, and overhang minimization, allowing the beam to be printed without conventional formwork. This digital-to-physical pipeline supports sustainable construction by reducing concrete volume, limiting steel reinforcement, and enabling rapid prefabrication aligned with environmentally responsive design practices.

Equilibrium geometry was generated through Polyhedral Graphic Statics [15, 16], facilitating the derivation of a force diagram optimized for post-tensioning cable alignment. The structural shell was

Proceedings of the IASS Annual Symposium 2025 The living past as a source of innovation

then articulated using diamond-type triply periodic minimal surfaces (TPMS) geometries, selected for their alignment with principal stress paths and their favorable printing characteristics. TPMS voids served dual purposes: increasing stiffness and forming continuous internal ducts for tendons [17, 18]. A signed distance function model [19, 20, 21] was used to fuse the funicular and TPMS geometries into a single printable solid, ensuring geometric and structural integration. Due to geometric complexity and the infeasibility of formwork, the beam was fabricated using a concrete extrusion system mounted on a 6-axis robotic arm. Spatial and material constraints required the beam to be divided into nine interlocking segments, assembled post-printing with internal ungrouted steel tendons. Each segment was printed individually, with segmentation planes optimized for mechanical interlocking and inspired by inverted stereotomic vaults.

To enhance printability, slicing planes were aligned with compressive stress trajectories, and toolpaths were optimized using a patch topology and dependency graph. This minimized tool retractions and improved layer continuity. Local offsetting techniques were applied to reduce unsupported overhangs. Segment fabrication times ranged from 10 to 20 minutes. The final beam measured about 10 meters in length, with a base width of 1.5 meters and a mid-span height of 0.8 meters. Post-tensioning was achieved using eight ungrouted 12.7-millimeter diameter steel cables. The modular approach supports repair, easy deconstruction, and material reuse, aligning with circular design strategies in contemporary construction.

2.2. Experimental setup

The structural performance of the full-scale post-tensioned 3D printed concrete canopy was evaluated through a four-point bending test conducted at CERIB's structural testing facility (Figure 1). The test specimen comprised nine prefabricated concrete segments assembled with eight ungrouted steel tendons, four placed near the top and four near the bottom, and bonded at the joints using Sikadur®-30 epoxy adhesive. The total span of the assembled element measured 9.05 m, with a clear span of 8.75 m between supports. Simply supported boundary conditions were simulated using a pin support and a roller support, each located 75 mm from the beam ends. Neoprene pads (6 mm thick) were placed at the supports to ensure uniform contact and minimize stress concentrations. Load was applied using two hydraulic actuators positioned symmetrically with respect to the mid-span at 3335 mm and 5555 mm from the left support, producing a 2220 mm loading span. Each actuator delivered half of the total load. To distribute the applied force uniformly across the beam width, two custom steel spreader beams (HEB140 over HEA350), each weighing approximately 335 kg and 300 mm wide, were placed at the loading points. Testing followed a displacement-controlled loading protocol.

Instrumentation included fifteen LVDTs to measure vertical displacements at mid-span, support points, and under the load application zones. Inclinometers were mounted on the spreader beams to monitor rotation and verify load uniformity. All data, load, displacement, and rotation, were continuously captured using a high-resolution data acquisition system throughout the test.

The beam was post-tensioned using eight T15S unbonded steel tendons arranged in two symmetrical layers, four near the top surface and four near the bottom. Each tendon had a diameter of 12.7 mm and a cross-sectional area of 150 mm², with a characteristic tensile strength of 1860 MPa. Tendons were housed in smooth plastic ducts embedded during printing, running continuously across all nine segments.

To induce a favorable stress distribution, top tendons were tensioned to 400 MPa and bottom tendons to 800 MPa. This differential post-tensioning introduced a compressive gradient along the beam depth, mitigating service-induced tensile stresses and enhancing flexural performance. All tendons were mechanically anchored at the beam ends.

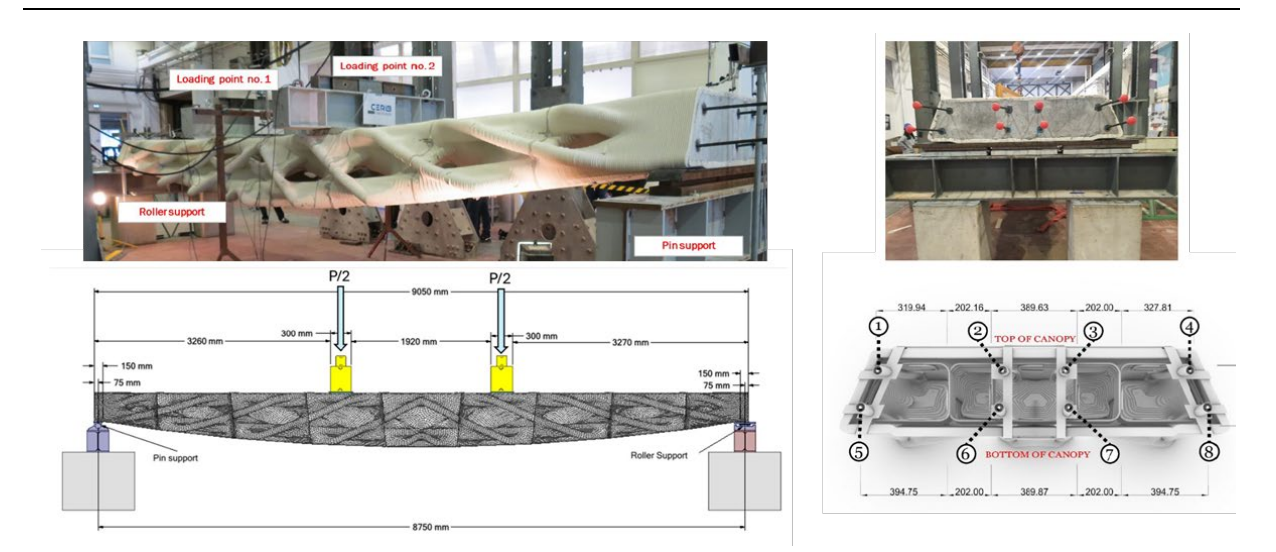


Figure 1. Experimental test setup

3. Finite element modeling

A 3D finite element model of the 9.05-meter post-tensioned concrete canopy was developed in ABAQUS. The model included eight steel tendons, four placed near the top and four near the bottom of the cross-section, to replicate the experimental post-tensioning scheme. Steel plates were modeled at both ends and tied to the concrete and tendon extremities. Boundary conditions were defined using a pin support on the left (fully constrained) and a roller support on the right (allowing only horizontal displacement). The analysis was conducted using a static general step with nonlinear geometry (NLGEOM) enabled to capture large deformations and potential geometric nonlinearities. Loading was applied in two stages. First, gravity loads (self-weight and dead loads) were introduced. Then, a four-point bending load was applied incrementally at the same locations as in the experimental setup to ensure consistency between simulation and testing.

3.1. Material

To simulate the nonlinear behavior of the 3D-printed post-tensioned concrete beam, the Concrete Damaged Plasticity (CDP) model in ABAQUS/Standard was utilized [12]. This model is well-suited for capturing the inelastic response of quasi-brittle materials such as concrete, particularly under cyclic or monotonic loading. The CDP framework accounts for both tensile cracking and compressive crushing with progressive stiffness degradation, allowing realistic simulation of damage evolution [22-25]. The concrete mix, developed by SIKA specifically for 3D printing with structural applications, was tested using standard cylindrical specimens under compressive and tensile loading (Figure 2). The results of these tests were used to calibrate the CDP input parameters. Table 1 summarizes the key mechanical properties and CDP parameters used in the FEM. The steel tendons were modeled as isotropic, linearly elastic elements, assuming they remained within the elastic range throughout loading. Material properties for the prestressing steel included a Young's modulus of 200 GPa, Poisson's ratio of 0.30, and a density of 7850 kg/m³.



(a) Compressive strength test

(b) Tensile strength test

Figure 2. Material tests on 3D printed cylindrical concrete specimens

Table 1. CDP model parameters for SIKA-based 3D printed concrete

Mass density (kg/m³)	Elastic material properties		CDP model					
	Modulus of elasticity (GPa)	Poisson's ratio	Ψ	е	$f_{ m b0}/f_{ m c0}$	K	Tensile strength (MPa)	Compressive strength (MPa)
2000	14	0.2	34	0.1	1.16	0.67	2	25

^{*} ψ : dilation angle; e: eccentricity; f_{bo}/f_{co} : biaxial-to-uniaxial compressive strength ratio; K: the ratio between the secondary stress constants in the tension and compression regions, and Viscosity parameter = 0.001.

3.2. Interaction and contact modeling

To simulate realistic behavior at key interfaces, appropriate interaction definitions were applied in the finite element model. The contact between post-tensioning tendons and surrounding concrete was modeled using ABAQUS's general contact algorithm, which is well-suited for complex geometries such as those found in 3D printed elements. Frictionless tangential behavior was assumed to avoid artificial shear transfer, while hard contact in the normal direction prevented penetration but allowed separation under tension. This setup reflects the behavior of unbonded tendons within smooth ducts. The beam was modeled as a monolithic structure, omitting segmentation and interfacial contacts to reduce computational complexity and improve convergence, especially at irregular mesh transitions. Rigid plates at the supports and loading points were connected to both the concrete and tendon surfaces using tie constraints. These ensured full kinematic compatibility, allowing proper load transfer and realistic simulation of anchorage and boundary conditions (Figure 3).

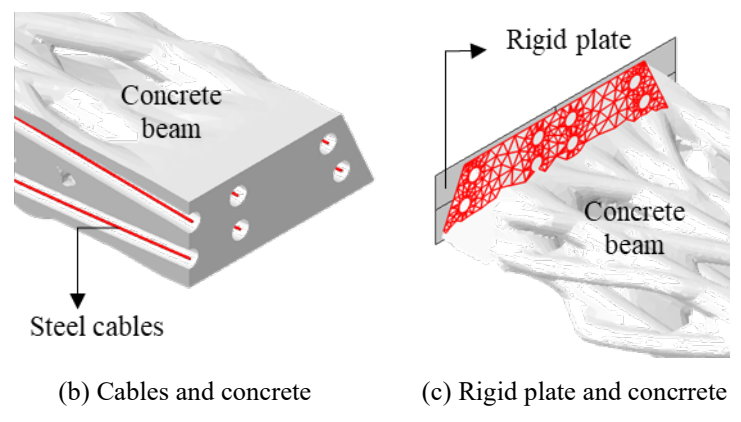


Figure 3. Interaction assumed in the FE model

3.2. Mesh strategy

The complex geometry of the 3D printed concrete beam, featuring internal voids, curved ribs, and organic contours, posed significant challenges for meshing directly within ABAQUS. To overcome these limitations, the volumetric mesh was generated using a Rhino-Grasshopper software plugin, then imported into ABAQUS as an orphan mesh. This approach enabled accurate tetrahedral meshing while preserving the design fidelity of the nine-segment beam. The concrete was discretized using C3D4, 4-node tetrahedral elements, totaling 418,760 elements. Once imported, the orphan mesh restricted further editing to assembly and interaction modules, while preserving the concrete mesh topology. Steel end plates, used for loading and support, were meshed natively in ABAQUS using a structured quadrilateral-dominated mesh with R3D4 rigid elements to ensure proper boundary condition implementation. The post-tensioning tendons were initially modeled with C3D10 quadratic tetrahedral elements. However, due to node selection limitations in ABAQUS with these elements, the cables were also converted into orphan meshes. This allowed full access to nodal data, enabling precise assignment of general contact conditions and tie constraints between tendons and concrete at the cable ends.

4. Results and discussion

Figure 4 presents a comparison between the experimental and numerical load-displacement responses based on displacement at mid-span, along with the corresponding deformed shape extracted from the finite element analysis. The overall behavior of the beam in both the experiment and FEM shows an initial linear response followed by nonlinear behavior with reduced stiffness, primarily attributed to progressive cracking and material degradation in the concrete. The numerical model accurately captured the initial stiffness and the general trend of the load-displacement curve. Slight deviations between the experimental and FEM curves became more pronounced at higher load levels, particularly beyond 60 kN. These differences are likely due to factors not fully captured in the model, for example material heterogeneity. The deformed shape from the FEM has the largest displacements occurred at mid-span, matching the results from the four-point bending test. The symmetry and smooth distribution of displacement also validate the appropriate implementation of boundary conditions and load application in the model. The maximum downward deflection reached approximately 50.74 mm in the simulation, which aligns closely with the experimental results.

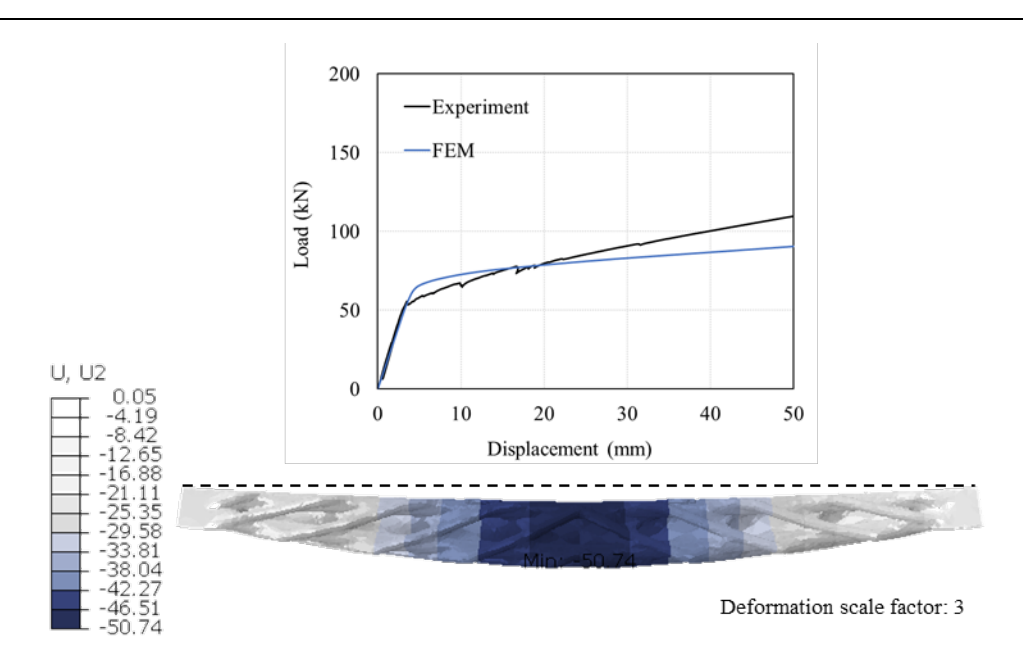


Figure 4. Load-displacement curve and deformation

Figure 5 shows the distribution of maximum (tensile) and minimum (compressive) principal stresses under peak loading conditions. As expected in a flexural system, tensile stresses (Figure 5a) concentrated along the lower mid-span, reaching a maximum of 1.95 MPa. These values align well with the material's tensile capacity and highlight the critical tension zones that could govern cracking behavior. The tensile stress fields were well-distributed, with no abrupt stress concentrations, indicating effective post-tensioning and continuity between segments. Compressive stresses (Figure 5b) were predominantly located along the upper mid-span and extended into the ribbed interior geometry. The maximum compressive stress reached -31.14 MPa, showing the high compressive demand carried by the upper region. The stress distribution followed the predicted funicular load path and confirmed the role of the TPMS-based geometry in efficiently channeling compressive forces while minimizing material volume.

In ABAQUS, the maximum principal plastic strain (PE) is commonly used to identify regions of accumulated tensile damage. Within the CDP model, elevated PE values signal areas prone to crack initiation and propagation under tensile stress. In this simulation, the maximum PE reached 0.33 and was concentrated around the mid-span, particularly in the middle segment, where geometric features and stress risers intensified strain localization (Figure 6). The resulting FE damage zones correspond closely with the physical test observations, including crack openings, delamination, and material rupture near the loading points. Although the numerical model does not explicitly represent the inter-segment joints, it successfully predicted the locations and patterns of failure observed in the experiment. The resulting damage zones underscore the dominant role of geometry and loading configuration in governing damage evolution, and they demonstrate the ability of a simplified, continuous model to replicate the global failure mechanisms of the assembled printed structure. However, it is important to acknowledge that modeling the beam as a monolithic entity omits the interfaces between individual segments. While this simplification improves computational efficiency and facilitates convergence, it may fail to capture localized stress concentrations and potential joint-related failures. In practice, interfacial discontinuities, adhesive bond behavior, and geometric imperfections at the joints can significantly influence stress redistribution and crack initiation. Therefore, future modeling efforts should incorporate detailed interface representations to more accurately assess localized behavior and

enhance predictive capability. It should also be noted that long-term effects such as creep, shrinkage, and fatigue were not considered in the current study, as they require time-dependent modeling approaches beyond the scope of this research. These phenomena merit further investigation to assess the durability and serviceability of 3D-printed post-tensioned structures under sustained and cyclic loading.

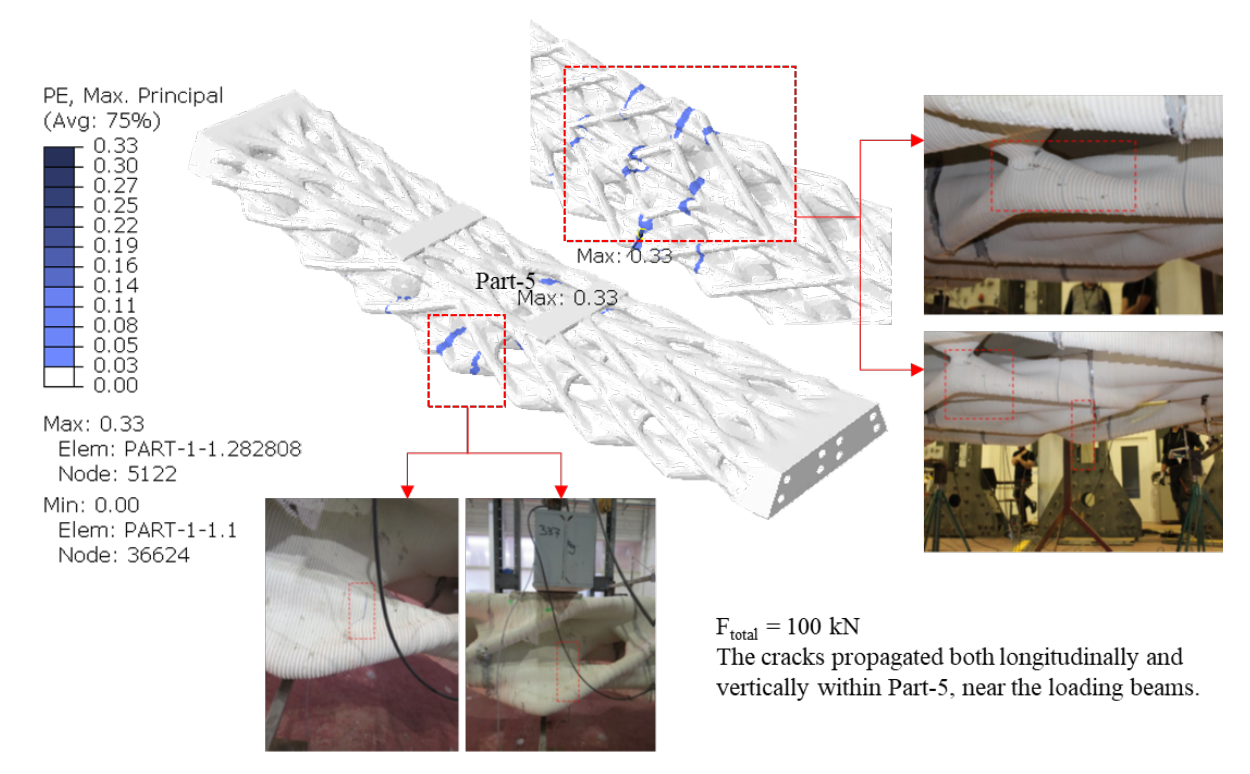


Figure 6. Crack propagation and failure mechanism

4. Conclusion

This study presents a numerical modeling framework for analyzing the structural behavior of a 3D-printed post-tensioned concrete structure. Using a computational workflow combining graphic statics, TPMS-based modeling, and additive manufacturing constraints, a structurally efficient and geometrically complex beam was developed and manufactured without conventional formwork. Experimental testing under four-point bending revealed flexural behavior, with the post-tensioning system effectively enhancing load capacity and controlling tensile cracking. Finite element analysis using the Concrete Damaged Plasticity (CDP) model closely replicated the beam's response, including displacement, stress distribution, and crack propagation. Despite modeling the beam as a continuous structure without segment interfaces, the numerical results successfully predicted the locations of observed failures, validating the simulation approach. The findings underscore the potential of combining digital design and robotic concrete 3D printing with post-tensioning to produce structurally optimized, prefabricated components. This approach offers a viable and sustainable path for future architectural and infrastructural applications, enabling reduced material use, efficient assembly, and high performance.

Acknowledgements

The authors acknowledge the support provided by SIKA and the Advanced Research Projects Agency Energy (ARPA-E) Grant of the U.S. Department of Energy (DE-AR0001631). This research was also partially funded by the National Science Foundation CAREER Award (NSF CAREER-1944691 CMMI) and the National Science Foundation Future Eco Manufacturing Research Grant (NSF, FMRG-CMMI 2037097) awarded to Masoud Akbarzadeh.

References

- [1] M. Buyle, J. Braet, and A. Audenaert. "Life cycle assessment in the construction sector: A review," *Renewable and sustainable energy reviews*, vol. 26, pp. 379-388, 2013.
- [2] M. S. Sandanayake. "Environmental impacts of construction in building industry, A review of knowledge advances, gaps and future directions," *Knowledge*, vol. 2. No. 1, pp. 139-156, 2022.
- [3] United Nations Environment Programme (UNEP). 2022 Global Status Report for Buildings and Construction: Towards a Zero-Emission, Efficient and Resilient Buildings and Construction Sector. Nairobi, 2022.
- [4] R. M. Andrew. "Global CO2 emissions from cement production," *Earth System Science Data*, vol. 10, no. 1, pp. 195-217, 2018.
- [5] S. A. Khan, M. Koç, and S. G. Al-Ghamdi. "Sustainability assessment, potentials and challenges of 3D printed concrete structures: A systematic review for built environmental applications," *Journal of Cleaner Production*, vol. 303, p. 127027, 2021.
- [6] T. Wangler, E. Lloret, L. Reiter, N. Hack, F. Gramazio, M. Kohler, ... and R. J. Flatt. "Digital concrete: opportunities and challenges," *Rilem technical letters*, vol. 1, no. 1, pp. 67-75, 2017.
- [7] D. Bolhassani, F. Yavartanoo, J.Tapia, M. Akbarzadeh, M. E. Ororbia, H. Chai,... and P. Kassabian. "The effect of post-tensioning on the behavior of small-scale 3D-printed concrete beams," *In Proceedings*, 2024.
- [8] G. Bai, J. Guan, L. Wang, Z. Li, and G. Ma. "Bending performance of 3D printed ultra high-performance concrete composite beams," *Additive Manufacturing*, vol. 89, p. 104298, 2024.
- [9] S. Raza, B. Manshadi, M. Sakha, R. Widmann, X. Wang, H. Fan and M. Shahverdi. "Load transfer behavior of 3D printed concrete formwork for ribbed slabs under eccentric axial loads," *Engineering Structures*, vol. 322, p. 119148, 2025.
- [10] F. Laccone, S. Menicagli, P. Cignoni and L. Malomo. "Computational design of segmented concrete shells made of post-tensioned precast flat tiles," *In Structures*, vol. 62, p. 106156, Elsevier, 2024.
- [11] Z. S. Miri, H. Baaj, and M. A. Polak. "3D-Printed concrete bridges: material, design, construction, and reinforcement," *Applied Sciences*, vol. 15, no. 6, p. 3054, 2025.
- [12] ABAQUS. "ABAQUS documentation", Dassault Syst'emes Simulia Corporation, Providence, RI, 2024.
- [13] M. Akbarzadeh, H.Chai, Y. Zhi, M. E. Ororbia, T. Teng, M. Bernhard... and B. Waligun. "Diamanti: 3D-printed, post-tensioned concrete canopy," Fabricate 2024: Creating Resourceful Futures, vol. 5, pp. 292-301, 2024.
- [14] H. Chai, Y. Lu, M. Hablicsek, and M. Akbarzadeh. "Generation of a compression-tension combined funicular polyhedral beam structure," *International Association for Shell and Spatial Structures (IASS)*, vol. 2023, no. 22, pp. 1-11, 2023.
- [15] M. Akbarzadeh. "3D graphical statics using reciprocal polyhedral diagrams," Doctoral dissertation, ETH Zurich, 2016.

Proceedings of the IASS Annual Symposium 2025 The living past as a source of innovation

- [16] J. Lee. "Computational design framework for 3D graphic statics," Doctoral dissertation, ETH Zurich, 2018.
- [17] H. A. Schwarz, and H. A. Schwarz. "Ueber die minimalfläche, deren begrenzung als ein von vier kanten eines regulären tetraeders gebildetes räumliches vierseit gegeben ist," *Gesammelte Mathematische Abhandlungen: Erster Band*, pp. 1-5, 1890.
- [18] A. H. Schoen. "Infinite periodic minimal surfaces without self-intersections," *National Aeronautics and Space Administration*, vol. 5541, 1970.
- [19] M. Bernhard, M. Hansmeyer, and B. Dillenburger. "Volumetric modelling for 3D printed architecture," *In AAG*, pp. 392-415, 2018.
- [20] J. F. Blinn. "A generalization of algebraic surface drawing," *ACM transactions on graphics* (TOG), vol. 1, no. 3, pp. 235-256, 1982.
- [21] M. Bernhard, M. Bolhassani, and M. Akbarzadeh. "Performative porosity-adaptive infills for concrete parts," *International Association of Shell and Spatial Structures*, 2021.
- [22] M. E. Ororbia, H. Chai, Y. Zhi, P. Vakhshouri, J. H. Chacon, J. Yost, ... and M. Akbarzadeh. "Experimental study of a funicular concrete beam prototype," *In Proceedings of the IASS 2024 Symposium*, 2024.
- [23] J. Lubliner, J. Oliver, S. Oller, and E. Onate. "A plastic-damage model for concrete," *International Journal of solids and structures*, vol. 25, no. 3, 299-326, 1989.
- [24] J. Lee, and G. L. Fenves. "Plastic-damage model for cyclic loading of concrete structures," *Journal of engineering mechanics*, vol. 124, no. 8, pp. 892-900, 1998.
- [25] M. Bolhassani, A. A. Hamid, A. C. Lau, & F. Moon. "Simplified micro modeling of partially grouted masonry assemblages," *Construction and Building Materials*, 83, 159-173, 2015.